Journal of Physics D: Applied Physics

PAPER • **OPEN ACCESS**

Reprogrammable metasurface design for NIR beam steering and active filtering

To cite this article: Hodjat Hajian *et al* 2024 *J. Phys. D: Appl. Phys.* **57** 415108

OPEN ACCESS
IOP Publishing

Journal of Physics D: Applied Physics

J. Phys. D: Appl. Phys. 57 (2024) 415108 (10pp)

https://doi.org/10.1088/1361-6463/ad626c

Reprogrammable metasurface design for NIR beam steering and active filtering

Hodjat Hajian[1,*], Matthieu Proffit[1], Ekmel Ozbay[2], Pascal Landais[3] and A Louise Bradley[1,4,*]

[1] School of Physics and AMBER, Trinity College Dublin, Dublin 2, Ireland
[2] Nanotechnology Research Center (NANOTAM), Institute of Materials Science and Nanotechnology (UNAM), Department of Physics, Department of Electrical and Electronics Engineering, Bilkent University, 06800 Ankara, Turkey
[3] School of Electronic Engineering, Dublin City University, Dublin 9, Ireland
[4] IPIC, Tyndall National Institute, Cork T12R5CP, Ireland

E-mail: hajianh@tcd.ie and bradlel@tcd.ie

Received 7 May 2024, revised 13 June 2024
Accepted for publication 12 July 2024
Published 24 July 2024

CrossMark

Abstract

Reprogrammable metasurfaces enable active modulation of light at subwavelength scales. Operating in the microwave, terahertz, and mid-infrared ranges, these metasurfaces find applications in communications, sensing, and imaging. Electrically tunable metasurfaces operating in the near-infrared (NIR) range are crucial for light detection and ranging (LiDAR) applications. Achieving a NIR reprogrammable metasurface requires individual gating of nano-antennas, emphasizing effective heat management to preserve device performance. To this end, here we propose an electrically tunable Au–vanadium dioxide (VO_2) metasurface design on top of a one-dimensional Si–Al_2O_3 photonic crystal (PC), positioned on a SiC substrate. Each individual Au–VO_2 nano-antenna is switched from an Off to ON state via Joule heating, enabling the programming of the metasurface using 1-bit (binary) control. While operating as a nearly perfect reflector at $\lambda_0 = 1.55\ \mu$m, the materials, thickness, and number of the layers in the PC are carefully chosen to ensure it acts as a thermal metamaterial. Moreover, with high optical efficiency ($R \sim 40\%$ at λ_0), appropriate thermal performance, and feasibility, the metasurface also enables broadband programmable beam steering in the $1.4 - 1.7\ \mu$m range for a wide steering angle range. This metasurface design also offers active control over NIR light transmittance, reflectance and absorptance in the wavelength range of $0.75 - 3\ \mu$m. These characteristics render the device practical for LiDAR and active filtering.

Supplementary material for this article is available online

Keywords: reprogrammable, metasurface, beam steering, near infrared, VO_2

1. Introduction

Beam steering at the near-infrared (NIR) and visible wavelengths has recently garnered substantial attention due to its vital importance in a range of technological applications, including light detection and ranging (LiDAR) [1], free-space optical communications [2], and holographic displays [3]. Wavefront engineering using optical phased arrays (OPAs) is accomplished through the control of phase and amplitude within the diffracted beam across antennas arranged in an array. Leveraging the interference of light scattered from each antenna within the array enables tailoring of radiated wavefronts to achieve a desired far-field intensity profile.

* Authors to whom any correspondence should be addressed.

Conventional OPAs alter the phase and amplitude of an input guided wave using phase shifters that are typically based on thermo-optic elements [4–6], micro-electro-mechanical systems (MEMS) [7–9] and p–i–n diodes phase modulators [10]. However, limited beam steering speed, mechanical failure rates, and the large inter-antenna spacing to avoid crosstalk between the adjacent elements reduces device reliability and limits the grating lobe-free steering range [11]. It has been demonstrated that beam steering with large field of view in conventional OPAs can be achieved by employing non-uniform antenna arrangements in sparse arrays. However, the noticeable amounts of background noise in the far-field radiation patterns still affects the device performance [12–14].

Alternatively, metasurfaces can be employed to achieve beam steering with an enhanced field of view. Metasurfaces are two-dimensional (2D) or planar versions of metamaterials and enable versatile wavefront control for scattered light [15, 16]. These phase arrays can be viewed as arrays of sub-wavelength antennas such that each antenna may impose a predefined phase shift, amplitude change, and polarization rotation on the scattered light [17]. Unlike the waveguide-based OPAs with large unit cell sizes, here only the fundamental beam can be generated by the metasurface due to the sub-wavelength feature of the unit cells. Another advantage of employing such metasurfaces for the beam steering application is the capability to excite the structure through out-of-plane illumination [15–17] rather than in-plane one [4–6] through a network of optical waveguides in traditional OPAs.

The control offered by metasurfaces over the properties of reflected or transmitted light, i.e. anomalous transmission or reflection, has given rise to the field of flat optics. This field investigates the potential applications of metasurfaces in developing compact optical components [18–20]. To date, phased array metasurfaces have been used to realize different categories of flat devices, namely beam splitters [17–20], focusing mirrors [21, 22], focusing lenses [23], holograms [24], and polarization converters [25, 26]. However, the aforementioned metasurfaces are passive, i.e. their properties are fixed at the time of the fabrication that limits their use in applications that require tunability. The ability to actively and dynamically tune the optical response of metasurfaces increases their functionality as dynamic beam splitters, holograms and lenses with reconfigurable focal lengths.

In the visible and NIR ranges, the tuning methods can be divided into two categories. Firstly, mechanical such as tunable lens using MEMS [27, 28] and stretchable metasurfaces [29]. These approaches are practical for relatively low tuning speed applications in a stable condition. In the second category, tunability at higher speed and efficiency is realized by employing active materials in the structure. The optical properties of these materials can be controlled by an external stimulus, such as optical laser pulses, applied bias voltage, or heating. The most common examples of these active materials are liquid crystals [30, 31], transparent conducting oxides, such as indium tin oxide (ITO) [32–39], III–V multiple-quantum-wells [40], or phase change materials (PCMs), such as chalcogenide glasses (GST, GSST) [41–46] and vanadium dioxide (VO_2) [47–57]. To achieve active metasurfaces for the mid-infrared and far-infrared ranges, graphene [58], GST [59] and VO_2 [42, 60–64] are potential candidates.

As a PCM, VO_2 undergoes a reversible insulator-to-metal transition (IMT) upon heating [65]. The IMT in VO_2 results in a significant change in its complex refractive index over a broad spectral range [66], occurring at $T_c = 341$ K close to the room temperature [67]. This feature makes this material a promising candidate for energy-efficient devices. In the majority of the studies on VO_2-based metasurfaces, the IMT was induced either by direct heating [47–57, 60–63] or by optical pumping [42, 64]. Another practical mechanism to achieve the IMT in VO_2 is electrical tuning [68]. Despite that the phase transition is still induced thermally, i.e. Joule heating, the electrical actuation provides a technology to separately address/gate each nano-antenna, enabling independent control of both the phase and amplitude of scattered light from individual meta-atom. This allows for realization of NIR reconfigurable phased array metasurfaces for active beam steering [69–72], a key requirement for chip-based LiDAR systems. It is worth noting that, unlike programmable VO_2-based metasurfaces operating in the microwave [23, 73], terahertz [72, 74], and mid-IR [59] ranges, two critical issues must be addressed when designing a NIR programmable device. These challenges arise due to limitations imposed by the size of the meta-atoms. (i) For the sake of addressability and feasibility, each VO_2-based meta-atom should have a geometrically simple structure, such as gratings. (ii) The heat generated through the gating mechanism should be effectively managed to maintain device performance, avoiding the need for additional complex cooling strategies.

It has been recently reported that a continuous phase shift of up to 250° at $\lambda \sim 1550$ nm can be obtained by a thermally tunable VO_2 nano-antenna reflect-array [70]. However, there is reduction in reflection from 25% in the dielectric phase of VO_2 (i-VO_2) to only 3% in the metallic phase of VO_2 (m-VO_2). The abrupt and nonlinear phase shift variation with temperature also makes controlling the intermediate states of VO_2 very challenging. Furthermore, the device exhibits thermal instability, caused by thermal crosstalk between adjacent nano-antennas and accumulation of heat inside the device caused by Joule heating [69].

To address these issues, a recent novel approach employed 1-bit (binary) control over each nano-antenna in a VO_2 reflect-array metasurface, while retaining control over the far-field pattern [71]. In that study, the metasurface is composed of 376 nm-thick metal–insulator–metal nano-antennas, separated from a bottom reflector by 600 nm-thick SiO_2 nano-pillars. The heat management within the structure ensures each antenna can be held in an insulator or metallic state independent of the neighboring antenna. The metasurface is capable of continuous beam steering over a 90° range at $\lambda_0 = 1550$ nm. However, the optical efficiency of the suggested design is low (reflectance, R, is 20%), and the design relies on deep narrow channels between the individual nano-antenna which can be challenging to fabricate.

Here, through a thermo-optical design approach, we propose an optically efficient ($R \sim 40\%$ at λ_0) and thermally stable metasurface for broadband NIR programmable beam steering and controlled light–matter interaction. The metasurface is composed of geometrically identical, hybrid Au–VO_2 nano-antennas on a one-dimensional photonic crystal (PC). The PC is composed of Si and Al_2O_3 layers and the whole structure is on a SiC substrate. The materials, thicknesses, and number of layers in the PC are carefully chosen to ensure heat management within the metasurface. This effectively transfers the heat produced by Joules heating of the Au nano-antennas to the SiC heat sink. In addition to its high optical efficiency, the thermal performance and fabrication simplicity, the metasurface exhibits broadband programmable beam steering in the range of $1.4\ \mu m < \lambda < 1.7\ \mu m$. It is also possible to achieve programmable light–matter interaction through the active control on the reflectance and absorptance of NIR light in the wavelength range of $0.75\ \mu m < \lambda < 3\ \mu m$. Furthermore, the presence of the PC provides the opportunity to shift the spectral location or filter the resonantly transmitted NIR light. These characteristics makes the designed device practical for a wide range of applications, including LiDAR, sensing, and filtering.

2. Results and discussion

2.1. Optical design of the reprogrammable metasurface beam steerer

In order to exhibit how the VO_2 metasurface array functions as a reprogrammable beam steerer, we first outline the geometry of a single unit cell of the metasurface for the i-VO_2 (figure 1(a) right) and m-VO_2 (figure 1(a) left) cases. Each unit cell is composed of a hybrid Au–VO_2 nano-antenna with thicknesses $t_{Au} = 0.1\ \mu m$ and $t_V = 0.1\ \mu m$, respectively, width $w = 0.25\ \mu m$ and periodicity p which is set to $\lambda_0/3.1 = 500$ nm for the operating free-space wavelength $\lambda_0 = 1.55\ \mu m$. The Au nano-antennas in the metasurface act as both plasmonic functional elements and the metallic contacts for actuation of the IMT of the VO_2 nano-antennas based on the Joule heating mechanism.

The hybrid Au–VO_2 nano-antennas sit on a PC that is composed of $N_{PC} = 5$ pairs of Si and Al_2O_3 layers with thicknesses $t_1 = 0.15\ \mu m$ and $t_2 = 0.15\ \mu m$, respectively. The whole structure is on a SiC substrate that acts as a transparent heat sink. Note that here $t_{1,2}$ is *not* taken as $\lambda_0/4n_{1,2}$ to ensure an effective heat transfer between the Au–VO_2 metasurface array and the SiC heat sink. This is further discussed in section 2.2.

The structure is designed and analyzed using finite difference time domain (FDTD) simulations [75], using refractive indices of Au, Si, and Al_2O_3 taken from [76], $n_{SiC} = 2.6$ [77] and VO_2 from [66] (see figure S1(a) in the supporting information). Reflectance (R) and transmittance (T) spectra of the bare PC (in the absence of the hybrid Au–VO_2 antennas) at normal incidence ($\theta_i = 0$) reveal that for different numbers of Si–Al_2O_3 pairs, the PC functions as a broadband reflector with an $R > 95\%$ over the wavelength range $1.36\ \mu m < \lambda_{BG} < 1.95\ \mu m$ and a narrowband reflector in the range $0.75\ \mu m < \lambda_{BG} < 0.88\ \mu m$ (see figure S2(a)). Here BG stands for photonic bandgap. From an optical perspective, N_{PC} significantly influences the number of resonances in the T and R spectra outside the bandgap regions. Despite a small reduction in the bandgap size at the target incident angle of 45° ($1.48\ \mu m < \lambda_{BG} < 1.75\ \mu m$), the bare PC ($N_{PC} = 5$, $t_{1,2} = 0.15\ \mu m$) maintains a $R > 95\%$ at the operating wavelength λ_0, as illustrated in figure 1(b). Figures S2(b) and S2(c) demonstrate that this observation holds true for $0 < \theta_i < 50°$. Consequently, the bare PC acts as a back reflector in the Au–VO_2 metasurface array at λ_0. It is noteworthy that due to the lossy nature of Si in the visible spectrum, the bare PC exhibits absorptive feature in the shaded region in figure 1(b). Moreover, from an optical perspective, using a Si–Al_2O_3 PC—instead of a thick Au layer as a bottom reflector—also allows for active control of transmittance at $\lambda > 0.75\ \mu m$. These aspects are deeply explored in section 3 of the supporting information.

Many potential applications of metasurfaces, such as beam steering, lensing, holography or structured light generation would require full 2π phase control [15–26]. However, in the concept of *digital metasurfaces*, it has been shown that by employing binary or 1-bit ('0' and '1') elements with only π phase shift it is possible to achieve beam steering (see e.g. [63]). In case of active control over the binary elements, *programmable metasurfaces* are realized [23]. In order to realize the required $\varphi = \pi$ radian phase coverage for the reflected light, we have performed single-element unit cell simulations for the i-VO_2 ($\alpha = 0$, $T = 331$ K, ε_i), m-VO_2 ($\alpha = 1$, $T = 365$ K, ε_m) and intermediate states of VO_2 ($0 < \alpha < 1$, ε_{int}) where α is the volume fraction and ε_{int}, at $\lambda_0 = 1.55\ \mu m$, is described by employing a Lorentz–Lorenz effective medium model as [70]

$$\frac{\varepsilon_{int} - 1}{\varepsilon_{int} + 2} = \alpha \frac{\varepsilon_m - 1}{\varepsilon_m + 2} + (1 - \alpha) \frac{\varepsilon_i - 1}{\varepsilon_i + 2}. \quad (1)$$

As it is observed from figure 1(c), for the i-VO_2 and m-VO_2 cases, corresponding to $\varphi = 0$ and $\varphi = \pi$, almost 40% reflectance is obtained, where the rest of power is lost due to Ohmic loss. These values exhibit almost two-fold enhancement of the reflectance efficiency compared to the previous VO_2 metasurface [71]. It is worth noting that the NIR VO_2-based metasurface discussed in [68] exhibits nearly 40% reflection efficiency, however, it lacks thermal performance due to the substantial accumulation of heat within the device. In contrast, the ITO-based metasurfaces discussed in [34–39] are notably suitable for beam steering applications, nevertheless, they demonstrate reflection efficiencies lower than 40%. The GST-based reprogrammable metasurface that is experimentally verified in [46] exhibit considerably high reflection contrast between the two different phases of GST. In contrast, our suggested device in this study shows small contrast in the reflected power for both the OFF (i-VO_2) and ON (m-VO_2) nano-antennas, demonstrating higher efficiency. For intermediate volume fractions, α, the phase varies smoothly

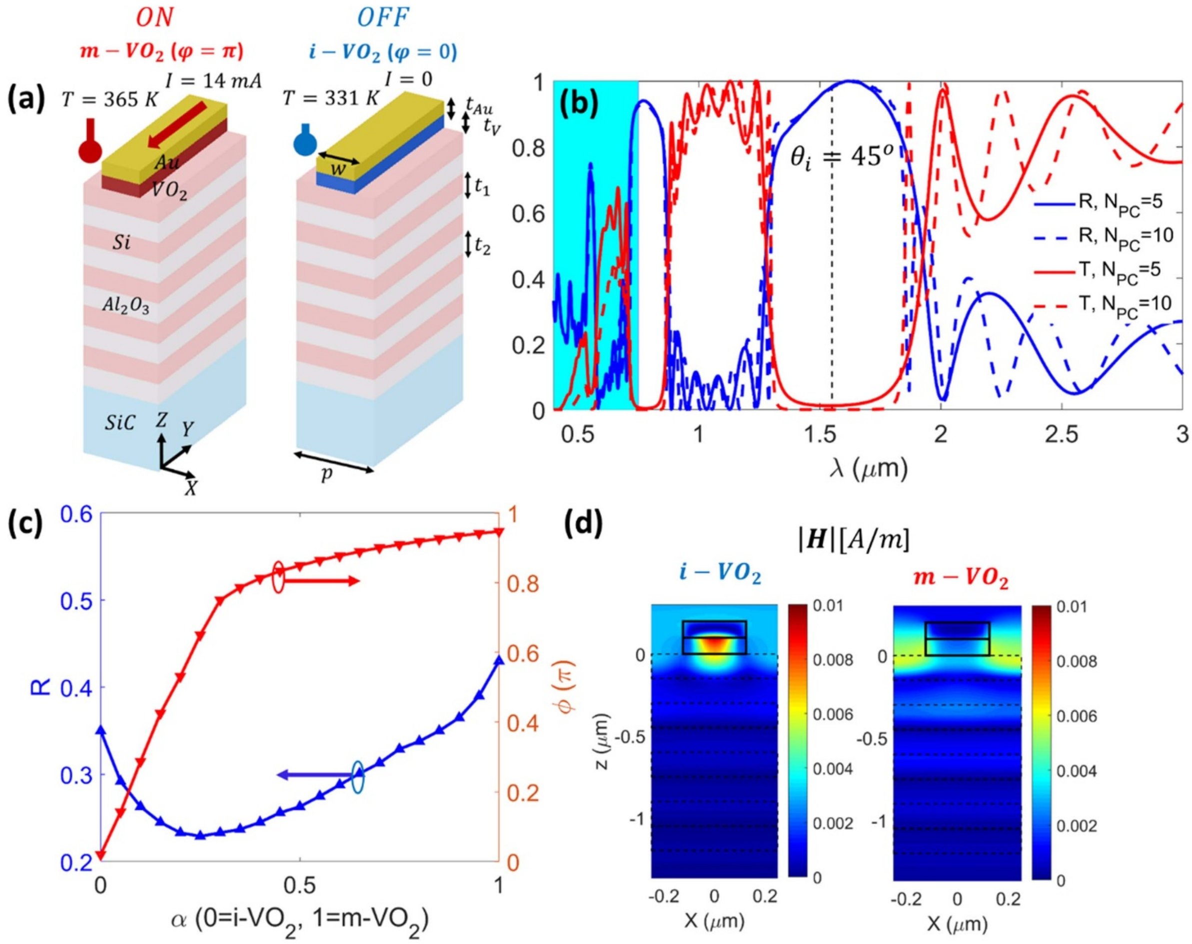

Figure 1. (a) Schematics of a unit cell of the VO_2 metasurface for the m-VO_2 (left, $T = 365$ K, $I = 14$ mA, and the red arrow indicates the current flow) and i-VO_2 (right, $T = 331$ K, $I = 0$) cases for $N_{PC} = 5$. Note that the hybrid Au–VO_2 nano-antennas are infinitely long along the y direction. Here, $t_{Au} = 0.1\ \mu$m, $t_V = 0.1\ \mu$m, $w = 0.25\ \mu$m and $p = \lambda_0/3.1$ where $\lambda_0 = 1.55\ \mu$m. (b) Reflectance [R (blue)] and transmittance [T (red)] spectra of the bare PC on the SiC substrate within $0.4 - 3\ \mu$m range at $\theta_i = 45°$. Solid and dashed curves represent the spectra for $N_{PC} = 5$ and 10, respectively, with $t_1 = t_2 = 0.15\,\mu$m. Highlighted region denotes the visible spectrum and the dashed vertical line highlights 1.55 μm. (c) Dependence of R and φ of x-polarized incident light for the unit cell shown in (a), on the i-VO_2 ($\alpha = 0$, OFF), m-VO_2 ($\alpha = 1$, ON) and intermediate states of VO_2 ($0 < \alpha < 1$) at λ_0 and $\theta_i = 45°$. (d) Corresponding side-view distributions of $|\boldsymbol{H}|$ in the unit cell for the i-VO_2 and m-VO_2 cases. The solid rectangles indicate the Au and VO_2 nano-antennas while the dashed rectangles represent locations of the Si and Al_2O_3 layers in the PC.

but the reflectance drops to 22% at $\alpha = 0.25$. However, since precise control of the intermediate volume factions of VO_2 is challenging in practice, we pick $\alpha = 0$ and $\alpha = 1$ for the binary design. The scattered light properties of the hybrid Au–VO_2 nano-antennas are tunable by the IMT of VO_2 via an active control on $|\boldsymbol{H}|$ and $|\boldsymbol{E}|$. This leads to the π phase difference between $\alpha = 0$ and $\alpha = 1$ cases. Figures 1(d) and S1(b) demonstrate a magnetic dipole resonance in the i-VO_2 case, as indicated by the significant enhancement of $|\boldsymbol{H}|$ and $|\boldsymbol{E}|$ within the VO_2 nano-antenna. Due to the metallic characteristic of VO_2 in the m-VO_2 case, both $|\boldsymbol{H}|$ and $|\boldsymbol{E}|$ are pushed outside of the nano-antennas denoting the support of a plasmonic lattice resonance [78]. As a result, rather than utilizing geometric phase gradient elements, we employ geometrically identical hybrid Au–VO_2 nano-antennas to obtain the phase control required for the beam steering applications. Note that here each Au–VO_2 nano-antenna can be separately gated using the employed gating technology in [37–39]. Furthermore, for the single-unit FDTD simulations discussed in figures 1(c) and (d), the periodic boundary condition is applied in the x direction. In contrast, for the simulations related to the array (e.g. figures 2(c1) and (d1)), the boundary conditions are chosen as perfectly matched layer.

According to the generalized Snell's law, for a *periodic* phase gradient metasurface with the phase variation in the x-direction, the relation between the angle of incidence θ_i and angle of anomalous reflection (steering angle) θ_r is [15, 16].

$$\sin(\theta_r) - \sin(\theta_i) = \pm\frac{1}{k_0 n}\frac{d\varphi(x)}{dx} \qquad (2a)$$

where $k_0 = \frac{2\pi}{\lambda_0}$, $d\varphi/dx$ is the phase gradient of the metasurface along the x-axis, and n is the refractive index of the surrounding medium (here $\theta_i = 45°$ and $n = 1$). With a phase range

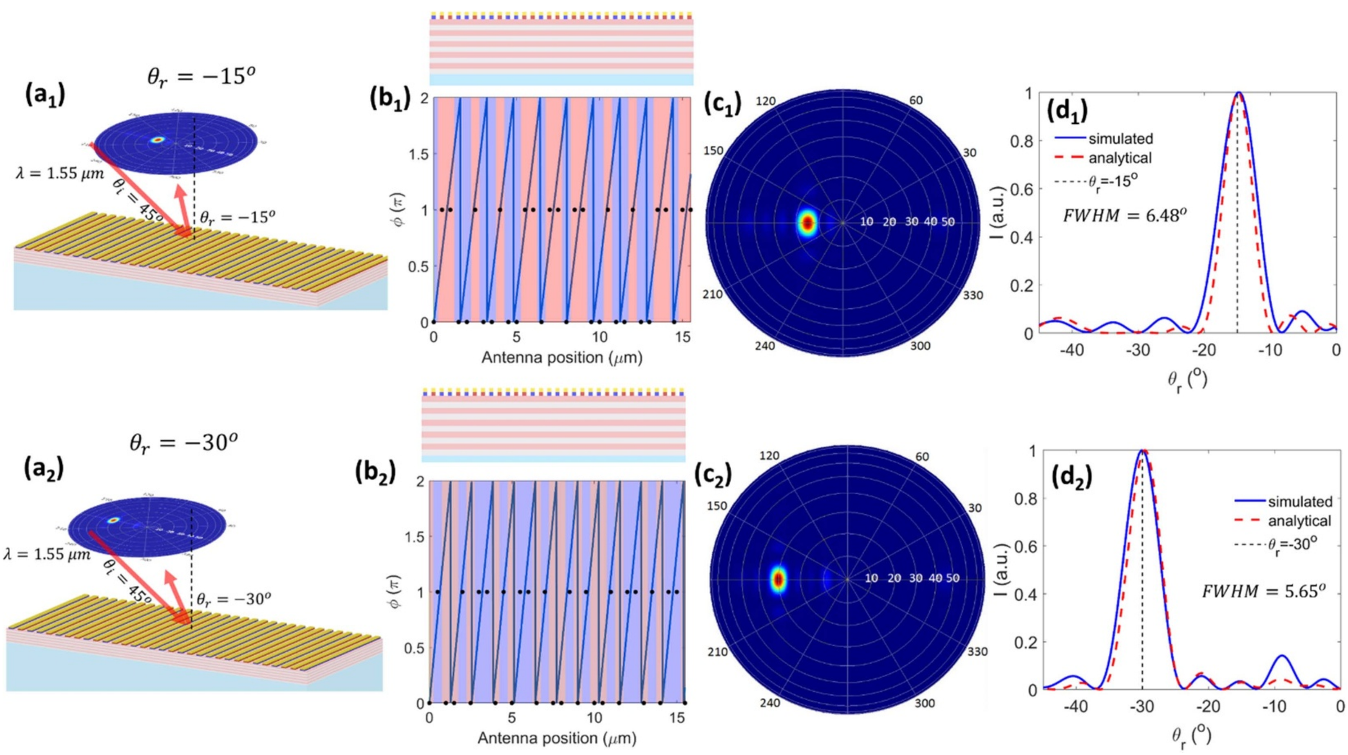

Figure 2. (a1) Perspective cartoon exhibiting the operation of the metasurface array composed of $N = 32$ hybrid Au–VO_2 nano-antennas ($N_{PC} = 5$) with $\theta_i = 45°$ and $\theta_r = -15°$. (b1) Continuous phase profile (solid blue) and the corresponding binary ON ($\varphi = \pi$ or m-VO_2) and OFF ($\varphi = 0$, i-VO_2) nano-antenna states for $\theta_r = -15^o$. Regions highlighted in pink and blue denote the ON and OFF states, respectively. Schematically shown on the top of the phase profile is the aperiodic arrangement of the ON (red) and OFF (blue) antennas along the array. FDTD calculated 3D (c1) and 2D (d1) far-field plots of $|E|^2$ of the scattered beam from the array for $\theta_i = 45°$ and $\theta_r = -15°$. In (d1), the dashed red curve exhibits the analytically calculated far-field response, and the vertical dashed line indicates $\theta_r = -15°$. Note that the dimension of the metasurface array is taken as $N.p \times N.p$ in the FDTD simulations related to (c1) and (d1). Figures (a2)–(d2) are similar to (a1)–(d1) while $\theta_i = 45°$ and $\theta_r = -30°$.

of 2π, equation (2) generates the continuous (ideal) phase profiles with a slope dictated by θ_r, shown by the solid blue lines in panels (b1) and (b2) of figure 2. This profile can be discretized using $\left|\frac{d\varphi(x)}{dx}\right| = \frac{2\pi}{m.p}$ for the case of a phase gradient metasurface, where $\Delta\varphi$ indicates the target 2π phase difference between the first and the *m*th meta-atom in each supercell [15, 16, 38]. However, for our *aperiodic* metasurface, we use a binary algorithm to further discretize the phase profile into an ensemble of $\varphi_{OFF} = 0$ and $\varphi_{ON} = \pi$ states. In this algorithm, $\varphi_{OFF} = 0$ (i-VO_2 or OFF state) is applied for $-\pi/2 < \varphi(x) < \pi/2$, and $\varphi_{ON} = \pi$ (m-VO_2 or ON state) is employed for $\pi/2 < \varphi(x) < 3\pi/2$ [71], where $\Delta\varphi = |\varphi_{ON} - \varphi_{FF}| = \pi$.

To elaborate further on how the binary algorithm works, we start with the investigation of the case of $\theta_i = 45^o$ and $\theta_r = -15^o$. Figure 2(a1) represents the perspective schematic of this case with the expected far-field response. Employing the binary algorithm on equation (2) for 32 antennas ($N = 32$), yields a binary phase profile that represents OFF/ON nano-antennas vs. their corresponding locations, as shown by black dots in figure 2(b1). Highlighted blue and pink areas indicate the OFF and ON states, respectively. The continuous phase profile is also plotted as the reference (solid blue lines) for ease of understanding. Alongside the phase profile, side-view schematic on the top exhibits how the OFF (blue) and ON (red) VO_2 nano-antennas are programmed in an aperiodic arrangement in accordance with the phase profile. FDTD calculated 3D and 2D far-field plots of the scattered $|\boldsymbol{E}|^2$ in figures 2(c1) and (d1). They clearly exhibit that the symmetry-broken arrangement of the nano-antenna, obtained by the binary algorithm, can successfully program the metasurface to generate an anomalously reflected beam at $\theta_r = -15^o$. In figure 2(d1), the FDTD calculated 2D far-field (solid blue curve) is compared with the analytical far-field response of the array calculated using

$$E(\theta) = E_{\mathrm{antenna}}(\theta)\sum_{m=1}^{N} \mathrm{e}^{\mathrm{i}(k_0 mp[\sin(\theta_i)+\sin(\theta)]+\Delta\varphi_m)}. \quad (3)$$

The agreement between the results verifies the consistency with the phased array theorem. Moreover, it is noteworthy that the full width at half maximum (FWHM) of the far-field response noticeably depends on *N*. Once figure 2(d1) is compared to figure S3 it is understood that by increasing the number of nano-antennas from 32 to 64, FWHM is decreased from 6.48° to 2.99°. Figures 2(a2)–(d2) show the results for an array configuration with $\theta_r = -30^o$. Moreover, to further investigate the beam steering characteristics of our binary metasurface design, the results related to $\theta_r = 15^o$, 30° and 0° are represented in figure S4 in supporting information. This dynamic control of the antenna arrangement for the operation at different θ_r makes the VO_2 metasurface suitable for the LiDAR application.

2.2. Thermal design of the device

As mentioned earlier, in our design, the top Au layer serves a dual role, acting as both plasmonic functional element and the contact of thermal actuation of the IMT of the VO_2 layer within each nano-antenna. This is achieved via the Joule heating mechanism by directing a DC current through the Au nano-antennas. Consequently, it is important to design a thermally stable device to avoid thermal crosstalk between adjacent antennas—so that they can be independently held in OFF or ON state—and realize proper cooling functionality. These criteria ensure consistent and reliable optical performance of the device, as well as mitigating potential issues related to thermal expansion, distortion, and other temperature-related factors. In this section, we perform Joule heating analysis using the heat transfer module of COMSOL Multiphysics, which solves the heat transfer equation [79]:

$$\rho C_p \frac{\partial T}{\partial t} - \nabla.(k\nabla T) = Q_e. \quad (4)$$

Here ρ, C_p, T, t, and k are density, heat capacity at constant pressure, temperature, time and thermal conductivity, respectively (see table 1 in supporting information). Note that in our calculations, k_{VO_2} and k_{SiC} are taken from [80] and [81], respectively. Q_e is the source of heat that is related to the DC current density and electrical conductivity as J^2/σ. Note that, in our analysis, a current of $I = 14$ mA flows through the Au nano-antennas for the ON (m-VO_2) states. Taking the width and thickness of the Au nano-antennas into account, this corresponds to a current density of 5.6×10^{11} A m^{-2} ($J = I/t_{Au}.w$) through the ON antennas and consequently 7.65×10^{15} W m^{-3} of heat is generated.

The left and right panels in figure 3(a) represent the steady-state thermal analysis of a single unit cell for the OFF and ON states, respectively. As seen from this figure, in the OFF state, the unit cell is kept at a minimum temperature of $T = 331$ K (i-VO_2), which is set as $T_c - 10$. On the other hand, in the ON state, the hybrid Au–VO_2 nano-antenna reaches a temperature of $T = 365$ K, ensuring the occurrence of the IMT (m-VO_2). These temperatures are well below and above the critical IMT temperature of VO_2 ($T_c = 341$), respectively. Furthermore, it is evident from the temperature profile in the ON state that the $N_{PC} = 5$, $150 - 150$ nm Si–Al_2O_3 PC effectively functions as a thermal metamaterial [82], efficiently transferring heat from the source (the Au nano-antenna) to the SiC heat sink. This point is supported by our analytical calculations once effective thermal conductivity of the PC is included in the investigation of the heat transfer mechanism between the source and the sink. It is noteworthy that SiC has been employed in electronic devices for cooling purposes due to its high thermal conductivity [81]. However, the advantage of using this material over Au is its transparency within the wavelength region of interest in this study, which provides our design with the flexibility to also control light transmission as discussed in section 3 of the supporting information.

Another important criterion that must be satisfied that thermal crosstalk between the adjacent nano-antennas does not influence the OFF–ON state of the antenna in the array. The steady state temperature profiles of the $N.p \times N.p$ binary metasurface array are illustrated in figures 3(b) and (c). Note that, in these temperature profiles, the ON and OFF antennas are gated in agreement with the schematically shown phase profiles (alongside these panels at the top) corresponding to the steering angles of $\theta_r = -15^o$ and $\theta_r = -30^\circ$. As seen from these panels, the thermal crosstalk between the adjacent ON–OFF antennas is negligible, guaranteeing that the ON antennas cannot thermally affect the OFF ones. Finally, transient simulations reveal the fast ON–OFF switching time of ~ 0.5 μs for each nano-antenna in the VO_2 metasurface, shown in figure 3(d). This demonstrates the capability of the proposed design for metasurface-enhanced dynamic beam steering and LiDAR technology [38, 39, 83]. This design may even find potential application as holographic light sources [84, 85], and also achromatic [86] and polychromatic [87] metadevices. Note that the thermal performance of the design has been analyzed through multi-physics simulations in COMSOL. To be specific, the Joule heating effect was induced by applying a current of 14 mA to the ON-state Au nano-antennas using AC/DC physics. The generated heat is analyzed using the heat transfer physics, utilizing a heat flux boundary condition with a heat transfer coefficient of 10 W $(m^2\,K)^{-1}$ applied to the top boundaries. Furthermore, the thermal isolation is applied to the side boundaries of the metasurface. Finally, the results are examined under both stationary and time-dependent scenarios. The results presented in figure 3(d) are derived from time-dependent analysis. Further investigation demonstrates that after $t > 0.5\,\mu$s, the time-dependent heat distributions converge to those obtained from stationary analysis.

It should be noted that the thickness of the layers and the number of the periods in the PC have a significant impact on the thermal performance of our design. Refractive index of the Si and Al_2O_3 are 3.48 and 1.74 at λ_0. Therefore, according to the wave optics theory, thickness of Si and Al_2O_3 layers in the PC is expected to be taken as $\lambda_0/4n_{1,2}$—i.e. 110 nm and 220 nm—to achieve a wide bandgap centered at λ_0. However, in figure S5, with $N_{PC} = 5$ and the mentioned thicknesses, it is evident that the PC no longer achieves the thermal requirements due to the reduced contribution of the highly conductive Si layers in the heat transfer of the device. In this case, the thermal crosstalk between the nano-antennas is considerably increased and the PC cannot properly transfer the heat between the source and the sink. The same issue happens while the number of the periods is increased to 10 in the $150 - 150$ nm Si–Al_2O_3 PC (see figure S6 in the supporting information).

In figure S7, it is proven that for the typical target reflection angles of $\theta_r = -15^o$ and $\theta_r = -30^o$, the metasurface can acts as a broadband beam steerer at the other wavelengths

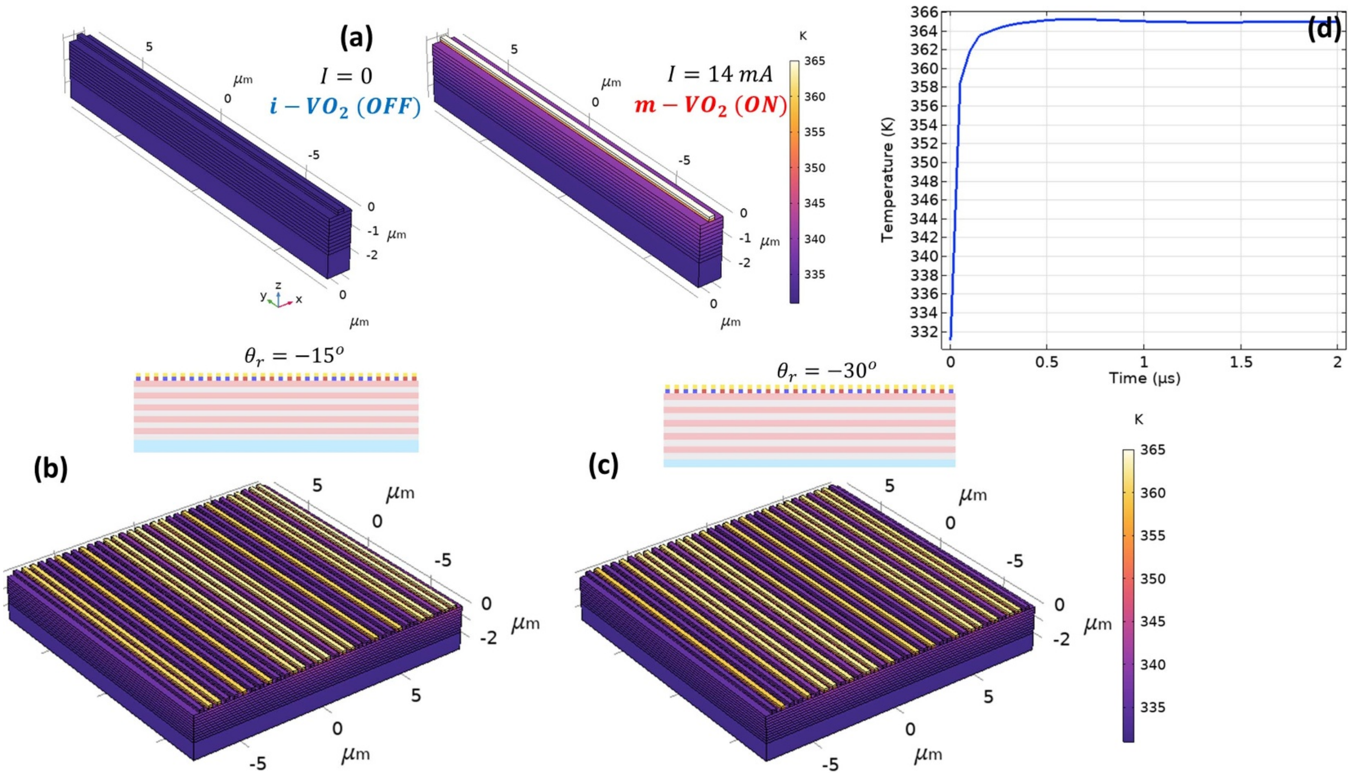

Figure 3. Thermal analysis of the VO_2 metasurface array for $N = 32$, $N_{PC} = 5$ and $t_1 = t_2 = 0.15$ μm. Steady-state temperature distribution of (a) a single unit cell and metasurface array for $\theta_r = -15°$ (b) and $\theta_r = -30°$ (c). For clarity, side-view schematics of the nano-antenna arrangements corresponding to the different phase profiles are also shown in (b) and (c). Note that the i-VO_2 (OFF) and m-VO_2 (ON) states correspond to $I = 0$ and $I = 14$ mA, respectively, and in the array simulations the dimensions are taken as $N.p \times N.p$. (d) Transient response of the array that shows the elements can reach to the ON state in less than 1 μs.

($\lambda = 1.45$ μm, 1.5 μm, 1.55 μm, 1.60 μm, and 1.65 μm) as well. Furthermore, as mentioned above, using a Si–Al_2O_3 PC, instead of a thick Au layer as a bottom reflector, allows for active control of the transmittance at $\lambda > 0.75$ μm. As discussed in figures S8 and S9 in the supporting information, this feature enables active control of light transmittance, reflectance, and absorptance within the wavelength range of 0.75 μm to 3 μm. This functionality renders the metasurface practical for active filtering and light absorption as well [88].

3. Conclusion

In conclusion, we have proposed a novel metasurface that is thermally practical and optically efficient, and is suitable for versatile applications involving broadband reprogrammable NIR beam steering, as well as absorption and filtering in reflection and transmission. The metasurface is composed of geometrically identical, hybrid Au–VO_2 nano-antennas on a Si–Al_2O_3 PC on a SiC substrate. The PC has been designed such that it acts as an almost perfect reflector at $\lambda_0 = 1.55$ μm and operates as a thermal metamaterial as well. That is, it provides for the heat management in the hybrid Au–VO_2 nano-antennas, making the reprogrammable metasurface. In other words, it effectively transfers the heat produced by the Au nano-antennas via the Joule heating to the SiC heat sink. The metasurface design, compatible with reduced complexity fabrication, has demonstrated high optical efficiency ($R \sim 40\%$ at the design wavelength of 1.55 μm) and thermal performance for broadband reprogrammable beam steering in the $1.4 - 1.7$ μm range over a wide angular range. Furthermore, it provides active control over NIR light transmittance, reflectance, and absorptance in the $0.75 - 3$ μm wavelength range. The exceptional characteristics of the proposed device show its versatility a wide range of applications, including LiDAR, optical communication, sensing and filtering.

Data availability statement

All data that support the findings of this study are included within the article (and any supplementary files).

Acknowledgments

This work was funded by Science Foundation Ireland (SFI) under Grants 21/FFP-P/10187, 16/IA/4550 and 12/RC/2278_2.

Conflict of interest

The authors declare no conflict of interest.

ORCID iDs

Hodjat Hajian https://orcid.org/0000-0001-6564-6273
A Louise Bradley https://orcid.org/0000-0002-9399-8628

References

[1] Schwarz B 2010 Lidar: mapping the world in 3D *Nat. Photon.* **4** 429–30
[2] Feng F, White I H and Wilkinson T D 2013 Free space communications with beam steering a two-electrode tapered laser diode using liquid-crystal SLM *J. Lightwave Technol.* **31** 2001–7
[3] Huang L, Zhang S and Zentgraf T 2018 Metasurface holography: from fundamentals to applications *Nanophotonics* **7** 1169–90
[4] Doylend J K, Heck M J R, Bovington J T, Peters J D, Coldren L A and Bowers J E 2011 Two-dimensional free-space beam steering with an optical phased array on silicon-on-insulator *Opt. Express* **19** 21595–604
[5] Yaacobi A, Sun J, Moresco M, Leake G, Coolbaugh D and Watts M R 2014 Integrated phased array for wide-angle beam steering *Opt. Lett.* **39** 4575–8
[6] Sun J, Timurdogan E, Watts M R, Hosseini E S and Yaacobi A 2013 Large-scale nanophotonic phased array *Nature* **493** 195–9
[7] Yoo B-W, Megens M, Chan T, Sun T, Yang W, Chang-Hasnian C J, Horsley D A and Wu M C 2013 Optical phased array using high contrast gratings for two dimensional beamforming and beamsteering *Opt. Express* **21** 12238–48
[8] Yoo B-W, Megens M, Sun T, Yang W, Chang-Hasnain C J, Horsley D A and Wu M C 2014 A 32×32 optical phased array using polysilicon sub-wavelength high-contrast-grating mirrors *Opt. Express* **22** 19029–39
[9] Chan T K, Megens M, Yoo B-W, Wyras J, Chang-Hasnain C J, Wu M C and Horsley D A 2013 Optical beam steering using an 8 × 8 MEMS phased array with closed-loop interferometric phase control *Opt. Express* **21** 2807–15
[10] Aflatouni F, Abiri B, Rekhi A and Hajimiri A 2015 Nanophotonic projection system *Opt. Express* **23** 21012–22
[11] Zadka M, Chang Y-C, Mohanty A, Phare C T, Roberts S P and Lipson M 2018 On-chip platform for a phased array with minimal beam divergence and wide field-of-view *Opt. Express* **26** 2528–34
[12] Hutchison D N, Sun J, Doylend J K, Kumar R, Heck J, Kim W, Phare C T, Feshali A and Rong H 2016 High-resolution aliasing-free optical beam steering *Optica* **3** 887–90
[13] Fatemi R, Khachaturian A and Hajimiri A 2019 A nonuniform sparse 2-D large-FOV optical phased array with a low-power PWM drive *IEEE J. Solid-State Circuits* **54** 1200–15
[14] Honari-Latifpour M, Binaie A, Eftekhar M, Madamopoulos N and Miri M 2022 Arrayed waveguide lens for beam steering *Nanophotonics* **11** 3679–86
[15] Yu N, Genevet P, Kats M A, Aieta F, Tetienne J-P, Capasso F and Gaburro Z 2011 Light propagation with phase discontinuities: generalized laws of reflection and refraction *Science* **334** 333
[16] Aieta F, Genevet P, Yu N, Kats M A, Gaburro Z and Capasso F 2012 Out-of-plane reflection and refraction of light by anisotropic optical antenna metasurfaces with phase discontinuities *Nano Lett.* **12** 1702
[17] Arbabi A, Horie Y, Bagheri M and Faraon A 2015 Dielectric metasurfaces for complete control of phase and polarization with subwavelength spatial resolution and high transmission *Nat. Nanotechnol.* **10** 937–43
[18] Yu N, Genevet P, Aieta F, Kats M A, Blanchard R, Aoust G, Tetienne J-P, Gaburro Z and Capasso F 2013 Flat optics: controlling wavefronts with optical antenna metasurfaces *IEEE J. Sel. Top. Quantum Electron.* **19** 4700423
[19] Kildishev A V, Boltasseva A and Shalaev V M 2013 Planar photonics with metasurfaces *Science* **339** 1289
[20] Yu N and Capasso F 2014 Flat optics with designer metasurfaces *Nat. Mater.* **13** 139–50
[21] Pors A, Nielsen M, Lynge Eriksen R and Bozhevolnyi S I 2013 Broadband focusing flat mirrors based on plasmonic gradient metasurfaces *Nano Lett.* **13** 829
[22] Ma Z, Hanham S M, Albella P, Ng B, Lu H T, Gong Y, Maier S A and Hong M 2016 Terahertz all-dielectric magnetic mirror metasurfaces *ACS Photonics* **3** 1010
[23] Cui T, Qi M Q, Wan X, Zhao J and Cheng Q 2014 Coding metamaterials, digital metamaterials and programmable metamaterials *Light Sci. Appl.* **3** 218
[24] Khorasaninejad M, Ting Chen W, Devlin R C, Oh J, Zhu A Y and Capasso F 2016 Metalenses at visible wavelengths: diffraction-limited focusing and subwavelength resolution imaging *Science* **352** 1190
[25] Wu P C, Tsai W-Y, Chen W T, Huang Y-W, Chen T-Y, Chen J-W, Liao C Y, Chu C H, Sun G and Tsai D P 2017 Versatile polarization generation with an aluminum plasmonic metasurface *Nano Lett.* **17** 445–52
[26] Liu X, Zhang X, Dong W, Liang Q, Ji C and Li J 2023 Broadband and high-efficiency polarization conversion with a nano-kirigami based metasurface *Sci. Rep.* **13** 7454
[27] Holsteen A L, Cihan A F and Brongersma M L 2019 Temporal color mixing and dynamic beam shaping with silicon metasurfaces *Science* **365** 257–60
[28] Arbabi E, Arbabi A, Kamali S M, Horie Y, Faraji-Dana M S and Faraon A 2018 MEMS-tunable dielectric metasurface lens *Nat. Commun.* **9** 812–9
[29] Zhang C, Jing J, Wu Y, Fan Y, Yang W, Wang S, Song Q and Xiao S 2020 Stretchable all-dielectric metasurfaces with polarization-insensitive and full-spectrum response *ACS Nano* **14** 1418–26
[30] Sautter J, Staude I, Decker M, Rusak E, Neshev D N, Brener I and Kivshar Y S 2015 Active tuning of all-dielectric metasurfaces *ACS Nano* **9** 4308
[31] Yu P, Li J and Liu N 2021 Electrically tunable optical metasurfaces for dynamic polarization conversion *Nano Lett.* **21** 6690
[32] Huang Y, Lee H W H, Sokhoyan R, Pala R A, Thyagarajan K, Han S, Tsai D P and Atwater H A 2016 Gate-tunable conducting oxide metasurfaces *Nano Lett.* **16** 5319–25
[33] Kafaie Shirmanesh G, Sokhoyan R, Pala R A and Atwater H A 2018 Dual-gated active metasurface at 1550 nm with wide (>300°) phase tunability *Nano Lett.* **18** 2957–63
[34] Forouzmand A, Salary M M, Inampudi S and Mosallaei H 2018 A tunable multigate indium-tin-oxide-assisted all-dielectric metasurface *Adv. Opt. Mater.* **6** 1701275
[35] Forouzmand A, Salary M M, Kafaie Shirmanesh G, Sokhoyan R, Atwater H A and Mosallaei H 2019 Tunable all-dielectric metasurface for phase modulation of the reflected and transmitted light via permittivity tuning of indium tin oxide *Nanophotonics* **8** 415–27
[36] Forouzmand A and Mosallaei H 2019 Electro-optical amplitude and phase modulators based on tunable guided-mode resonance effect *ACS Photonics* **6** 2860–9
[37] Kafaie Shirmanesh G, Sokhoyan R, Chieh Wu P and Atwater H A 2020 Electro-optically tunable multifunctional metasurfaces *ACS Nano* **14** 6912–20

[38] Thureja P, Kafaie Shirmanesh G, Fountaine K T, Sokhoyan R, Grajower M and Atwater H A 2020 Array-level inverse design of beam steering active metasurfaces *ACS Nano* **14** 15042–55
[39] Park J *et al* 2021 All-solid-state spatial light modulator with independent phase and amplitude control for three-dimensional LiDAR applications *Nat. Nanotechnol.* **16** 69
[40] Wu P C, Pala R A, Kafaie Shirmanesh G, Cheng W-H, Sokhoyan R, Grajower M, Alam M Z, Lee D and Atwater H A 2019 Dynamic beam steering with all-dielectric electro-optic III–V multiple-quantum-well metasurfaces *Nat. Commun.* **10** 3654
[41] Zou L, Cryan M and Klemm M 2014 Phase change material based tunable reflectarray for free-space optical inter/intra chip interconnects *Opt. Express* **22** 24142–8
[42] Wang Q, Rogers E T F, Gholipour B, Wang C M, Yuan G, Teng J and Zheludev N I 2016 Optically reconfigurable metasurfaces and photonic devices based on phase change materials *Nat. Photon.* **10** 60–65
[43] Yin X, Steinle T, Huang L, Taubner T, Wuttig M, Zentgraf T and Giessen H 2017 Beam switching and bifocal zoom lensing using active plasmonic metasurfaces *Light Sci. Appl.* **6** e17016
[44] Galarreta C R, Alexeev A M, Au -Y-Y, Lopez-Garcia M, Klemm M, Cryan M, Bertolotti J and Wright C D 2018 Nonvolatile reconfigurable phase-change metadevices for beam steering in the near infrared *Adv. Funct. Mater.* **28** 1704993
[45] Abed O and Yousefi L 2020 Tunable metasurfaces using phase change materials and transparent graphene heaters *Opt. Express* **28** 33876–89
[46] Abdollahramezani S *et al* 2022 Electrically driven reprogrammable phase-change metasurface reaching 80% efficiency *Nat. Commun.* **13** 1696
[47] Kaplan G, Aydin K and Scheuer J 2015 Dynamically controlled plasmonic nano antenna phased array utilizing vanadium dioxide [Invited] *Opt. Mater. Express* **5** 2513–24
[48] Rensberg J *et al* 2016 Active optical metasurfaces based on defect-engineered phase-transition materials *Nano Lett.* **16** 1050–5
[49] Zhu Z, Evans P G, Haglund R F Jr and Valentine J G 2017 Dynamically reconfigurable metadevice employing nanostructured phase-change materials *Nano Lett.* **17** 4881
[50] Dong K *et al* 2018 A lithography-free and field-programmable photonic metacanvas *Adv. Mater.* **30** 1703878
[51] Howes A, Zhu Z, Curie D, Avila J R, Wheeler V D, Haglund R F and Valentine J G 2020 Optical limiting based on Huygens' metasurfaces *Nano Lett.* **20** 4638–44
[52] Tripathi A *et al* 2021 Tunable Mie-resonant dielectric metasurfaces based on VO_2 phase-transition materials *ACS Photonics* **8** 1206
[53] Kepič P, Ligmajer F, Hrtoň M, Ren H, Menezes L D S, Maier S A and Šikola T 2021 Optically tunable Mie resonance VO_2 nanoantennas for metasurfaces in the visible *ACS Photonics* **8** 1048–57
[54] Boyce A M, Stewart J W, Avila J, Shen Q, Zhang S, Wheeler V D and Mikkelsen M H 2022 Actively tunable metasurfaces via plasmonic nanogap cavities with sub-10-nm VO_2 films *Nano Lett.* **22** 3525
[55] Wilson K, Marocico C A and Bradley A L 2018 Dynamic structural colour using vanadium dioxide thin films *J. Phys. D: Appl. Phys.* **51** 255101
[56] Cunningham S and Bradley A L 2022 Tunable plasmonics with Au nanoparticles coupled to thin film vanadium dioxide *Opt. Mater. Express* **12** 3638–47
[57] Cunningham S, Hrelescu C and Bradley A L 2021 Plasmonic nanodiscs on vanadium dioxide thin films for tunable luminescence enhancement *Opt. Express* **29** 22288
[58] Li Z, Yao K, Xia F, Shen S, Tian J and Liu Y 2015 Graphene plasmonic metasurfaces to steer infrared light *Sci. Rep.* **5** 12423
[59] Leitis A, Heßler A, Wahl S, Wuttig M, Taubner T, Tittl A and Altug H 2020 All-dielectric programmable Huygens' metasurfaces *Adv. Funct. Mater.* **30** 1910259
[60] Dicken M J, Aydin K, Pryce I M, Sweatlock L A, Boyd E M, Walavalkar S, Ma J and Atwater H A 2009 Frequency tunable near-infrared metamaterials based on VO_2 phase transition *Opt. Express* **17** 18330–9
[61] Kats M A, Blanchard R, Zhang S, Genevet P, Ko C, Ramanathan S and Capasso F 2013 Vanadium dioxide as a natural disordered metamaterial: perfect thermal emission and large broadband negative differential thermal emittance *Phys. Rev.* X **3** 041004
[62] Kocer H, Butun S, Banar B, Wang K, Tongay S, Wu J and Aydin K 2015 Thermal tuning of infrared resonant absorbers based on hybrid gold-VO_2 nanostructures *Appl. Phys. Lett.* **106** 161104
[63] Erçağlar V, Hajian H, Serebryannikov A E and Ozbay E 2021 Multifunctional tunable gradient metasurfaces for terahertz beam splitting and light absorption *Opt. Lett.* **46** 3953
[64] Liu M *et al* 2012 Terahertz-field-induced insulator-to-metal transition in vanadium dioxide metamaterial *Nature* **487** 345–8
[65] Imada M, Fujimori A and Tokura Y 1998 Metal-insulator transitions *Rev. Mod. Phys.* **70** 1039
[66] Wan C *et al* 2019 optical properties of thin-film vanadium dioxide from the visible to the far infrared *Ann. Phys.* **531** 1900188
[67] Qazilbash M M *et al* 2007 Mott transition in VO_2 revealed by infrared spectroscopy and nano-imaging *Science* **318** 1750–3
[68] Markov P, Marvel R E, Conley H J, Miller K J, Haglund R F Jr and Weiss S M 2015 Optically monitored electrical switching in VO_2 *ACS Photonics* **2** 1175–82
[69] Kim M, Jeong J, Poon J K S and Eleftheriades G V 2016 Vanadium-dioxide-assisted digital optical metasurfaces for dynamic wavefront engineering *J. Opt. Soc. Am.* B **33** 980–8
[70] Kim Y, Wu P C, Sokhoyan R, Mauser K, Glaudell R, Kafaie Shirmanesh G and Atwater H A 2019 Phase modulation with electrically tunable vanadium dioxide phase-change metasurfaces *Nano Lett.* **19** 3961–8
[71] Proffit M, Pelivani S, Landais P and Bradley A L 2022 Electrically driven reprogrammable vanadium dioxide metasurface using binary control for broadband beam steering *ACS Appl. Mater. Interfaces* **14** 41186
[72] Hashemi M M, Yang S, Wang T, Sepúlveda N and Jarrahi M 2016 Electronically-controlled beam steering through vanadium dioxide metasurfaces *Sci. Rep.* **6** 35439
[73] Saleem M, Irfan M, Alanazi M A and Atiq S 2023 2–bit programmable metasurface for low radar cross section antenna and beam steering applications *Radio Sci.* **58** e2023RS007767
[74] Yang D, Wang W, Lv E, Wang H, Liu B, Hou Y and Chen J-H 2022 Programmable VO_2 metasurface for terahertz wave beam steering *iScience* **25** 104284
[75] Lumerical Inc. (available at: www.lumerical.com/tcadproducts/fdtd)
[76] Palik E D 1988 *Handbook of Optical Constants of Solids* (Elsevier)
[77] Singh S, Potopowicz J R, Van Uitert L G and Wemple S H 1971 Nonlinear optical properties of hexagonal silicon carbide *Appl. Phys. Lett.* **19** 53–56
[78] Bin-Alam M S *et al* 2021 Ultra-high-Q resonances in plasmonic metasurfaces *Nat. Commun.* **12** 974
[79] COMSOL Heat transfer interface documentation (available at: www.comsol.com/heat-transfer-module)

[80] Kizuka H, Yagi T, Jia J, Yamashita Y, Nakamura S, Taketoshi N and Shigesato Y 2015 Temperature dependence of thermal conductivity of VO_2 thin films across metal–insulator transition *Jpn. J. Appl. Phys.* **54** 053201
[81] Parkand K and Bayram C 2016 Thermal resistance optimization of GaN/substrate stacks considering thermal boundary resistance and temperature-dependent thermal conductivity *Appl. Phys. Lett.* **109** 151904
[82] Li Y, Li W, Han T, Zheng X, Li J, Li B, Fan S and Qiu C 2021 Transforming heat transfer with thermal metamaterials and devices *Nat. Rev. Mater.* **6** 488
[83] Juliano Martins R *et al* 2022 Metasurface-enhanced light detection and ranging technology *Nat. Commun.* **13** 5724
[84] Li G, Clarke B P, So J, MacDonald K F and Zheludev N I 2016 Holographic free-electron light source *Nat. Commun.* **7** 13705
[85] Ou K, Li G, Li T, Yang H, Yu F, Chen J, Zhao Z, Cao G, Chen X and Lua W 2018 High efficiency focusing vortex generation and detection with polarization-insensitive dielectric metasurfaces *Nanoscale* **10** 19154
[86] Ou K *et al* 2020 Mid-infrared polarization-controlled broadband achromatic metadevice *Sci. Adv.* **6** eabc0711
[87] Chen J *et al* 2023 Polychromatic full-polarization control in mid-infrared light *Light Sci. Appl.* **12** 105
[88] Hajian H, Ghobadi A, Butun B and Ozbay E 2019 Active metamaterial nearly perfect light absorbers: a review *J. Opt. Soc. Am.* B **36** F131–43